Tribology International 154 (2021) 106671

Contents lists available at ScienceDirect

Tribology International

journal homepage: http://www.elsevier.com/locate/triboint

Approximating the influence coefficients of non-planar elastic solids for conformal contact analysis

Julio Blanco-Lorenzo [a,*], Edwin A.H. Vollebregt [b], Javier Santamaria [a], Ernesto G. Vadillo [a]

[a] Mechanical Engineering Department, University of the Basque Country UPV/EHU, Plaza Ingeniero Torres Quevedo 1, 48013, Bilbao, Spain
[b] Vtech CMCC, Bahialaan 100, 3065 WC, Rotterdam, the Netherlands

ARTICLE INFO

Keywords:
Non-planar solids
Influence coefficients
Conformal contact
Exact contact theory

ABSTRACT

The exact contact theory is an efficient alternative to the more general yet computationally expensive Finite Element Method for the detailed study of elastostatic contact problems. For its application in conformal contact problems, the exact contact theory needs to be fed with influence coefficients (ICs) appropriate for non-planar solids. An analytical approximation of the ICs for non-planar solids was proposed in a previous work, avoiding the involved process generally necessary to obtain ICs accurately. This work presents further developments of this approximation, further comparison with numerically obtained ICs, and evaluates the errors incurred when using approximated ICs in conformal contact.

1. Introduction

Conformal contact between solid bodies is present in numerous engineering applications. Its numerical study may be undertaken by means of the Finite Element Method (FEM), that can incorporate advanced features in the analysis in a precise way, such as large deformations, complex material and contact interface behaviour, and dynamic effects. Many examples may be found in the literature of the application of FEM in the study of contact related phenomena; [1–5] are some related to the wheel–rail application.

Contact problems are particularly highly non-linear and require significant computer resources to solve, as stated in Ref. [6]. A high level of refinement is needed around the contact patch to obtain valid contact solutions, representing the relationship between the local contact stress and displacement fields adequately. Consequently, FE models used for 3D contact mechanics analyses often reach sizes of the order of the million degrees of freedom. The exact contact theory developed by Kalker [7], and implemented in the program CONTACT [8–10] as well as in later codes by other researchers (e.g. Refs. [11–13]), is a convenient alternative that allows for the efficient and yet precise modelling of a wide range of 2D and 3D contact problems, either frictionless or with friction, static or rolling, and steady state or transient. Since it is a Boundary Element Method, in which the contact surface is discretized rather than the volume of the contacting bodies, its computational costs in the solution of large elastostatic, small-displacement, concentrated contact problems are far lower than those of FEM, especially when detailed results at the contact surface are sought.

The exact contact theory is most conveniently applied to elastostatic concentrated contact problems using the half-space approach. In recent years, several groups ([14–19]) aimed at extending its applicability to conformal contact problems, focusing especially in the wheel–rail case. The main obstacle hindering this is the difficulty in obtaining the influence coefficients (ICs) that characterize the mechanical behaviour of general non-planar bodies. These are not readily available as are the elastic half-space ICs for concentrated contact problems, known in analytical form. The numerical computation of the ICs of non-planar solids with FEM was addressed in previous works [14,15,20]. This is a cumbersome strategy involving long FE computations and large files specific to each contact configuration. On the other hand, an analytical approximation was proposed in Ref. [18] as a fast approach for ICs for non-planar bodies. This work presents further developments on this.

The paper is organized as follows. Section 2 reviews the concept of ICs and their role in the formulation of contact problems with the exact contact theory. The earlier analytical approximation for the ICs of non-planar bodies is revisited in Section 3, discussing its similarity with the ICs for cylindrical geometries, and proposing two new approximations on the basis of surface orientations. An extension for the approximated ICs is presented in Section 4, aimed particularly at improving their

* Corresponding author.
E-mail addresses: julio_blanco001@ehu.es (J. Blanco-Lorenzo), edwin.vollebregt@cmcc.nl (E.A.H. Vollebregt), javier.santamaria@ehu.eus (J. Santamaria), ernesto.garciavadillo@ehu.es (E.G. Vadillo).

https://doi.org/10.1016/j.triboint.2020.106671
Received 17 June 2020; Received in revised form 3 September 2020; Accepted 17 September 2020
Available online 23 September 2020

performance in the tangential part of the contact problem. Numerical results are given in Section 5, on the precision of the approximated ICs for two sample non-planar wheels and rails with different cross sections, and in Section 6, on the errors made in the solution of conformal contact problems. The numerical examples presented illustrate wheel–rail contact situations, but the approach is valid also in other applications where conformal contact is found, such as in rolling bearings. The main findings of the work are summarized in Section 7.

2. The influence coefficients in contact problems

The Influence Functions (IFs) state the relationship between inputs and responses in continuum systems, and the Influence Coefficients (ICs) are their equivalents in discrete systems with multiple degrees of freedom. In contact mechanics, the attention is focused on the IFs which relate the surface displacements **u** to the transmitted stresses **p** in the contact surface, since both magnitudes enter directly in the contact problem formulation. These are the quantities with which this work is concerned. In linear elasticity, the relationship between **u** and **p** may generally be expressed as indicated in Eq. (1).

$$u_i(\mathbf{x}) = \sum_j \iint_{S\in C} \mathrm{i}_{ij}(\mathbf{x},\mathbf{x}')p_j(\mathbf{x}')dS(\mathbf{x}'), \quad i,j \in \{x,s,n\} \tag{1}$$

The different quantities in Eq. (1) are expressed on a right-handed curvilinear coordinate system with orthogonal axes $\{x,s,n\}$ defined on the contact surface, with x and s directions tangent to its surface, and n direction normal to it. i_{ij} is the influence function which relates the surface displacement in direction i, u_i, to the applied point load in direction j, $p_j dS$. i_{ij} depends on the elastic constants and geometry of the solid, and in general, on the positions $\mathbf{x}'$ where the load is applied and $\mathbf{x}$ where the displacement is observed. Using similarity, the dependence on $\mathbf{x}$ and $\mathbf{x}'$ may be replaced in the elastic half-space by a dependence on relative position $\mathbf{x}-\mathbf{x}'$.

The integral in Eq. (1) is extended only over the part of the surface of the solid S which enters in contact, neglecting the contribution of other loads which may be acting on the solid to the displacement gradients in the neighbourhood of the contact region C. This is applicable in cases in which the contact region is much smaller than the overall dimensions of the solid, and the local contact problem on the one hand and the global structural problem of the solid on the other hand may be considered uncoupled.[1]

Equation (1) is discretized into Eq. (2) by dividing the contact surface C (or a bigger part of S encompassing C) into a mesh of N elements. Here $\Im_{IiJj}$ is the influence coefficient relating the displacement in direction i at element I to the load in direction j at element J, and $\mathbf{x}_I$, $\mathbf{x}_J$ are the positions of the I^{th} and J^{th} elements of the discretization. The determination of the ICs $\Im_{IiJj}$ is necessary to complete the exact contact theory formulation of the contact problem. They are obtained by a convolution of the corresponding $\mathrm{i}_{ij}(\mathbf{x}_I,\mathbf{x}')$ with a given load shape function in surface element J. Piecewise constant and bilinear shape functions are usually employed, as discussed in Refs. [8,22] for instance.

$$u_i(\mathbf{x}_I) = \sum_j \sum_{J=1}^{N} \Im_{IiJj}(\mathbf{x}_I,\mathbf{x}_J)p_j(\mathbf{x}_J), \quad i,j \in \{x,s,n\}, \quad I,J \in \{1\ldots N\} \tag{2}$$

[1] There are cases in which remote actions produce significant deformations at the contact level, such as in the 2D problem of a pin on a closely conforming hole as studied in Ref. [21]. If remote actions are not altered by the particular contact solution then both problems may be treated separately by superposition, incorporating the contribution of the remote actions on the initial "undeformed" configuration for the contact problem. On the other hand, if remote actions do depend on the particular contact stress distribution (e.g. if they are displacement-controlled), both problems have to be solved together.

In concentrated contact problems, the dimensions of the contact patch are much smaller than the curvature radii of the contacting surfaces, and hence the contact surface may be approximated as planar. A possible discretization for this case is shown in Fig. 1a, together with an element displacement u_{In} and load p_{Jn} concerned with the IC $\Im_{InJn}$. The smallness of the contact patch with respect to the global dimensions of the contacting solids, together with the flatness of the contact surface, bring an important advantage regarding the computation of the ICs: the mechanical behaviour of each of the contacting solids in the vicinity of the contact may be approximated by that of a half-space. This implies that half-space ICs, which are known analytically, may be applied in such contact problems, regardless of the overall geometry or supporting conditions of the contacting solids.

In contrast, when contact occurs between two closely conforming surfaces, the contact region may extend over a large portion of the surfaces. The contact surface may become curved, and the half-space approach may not be applicable anymore. Fig. 1b shows an example geometry of such a case with a curved contact surface. The local $\{x,s,n\}$ directions of elements I and J are represented in the figure, noting that they have different orientations. In general, all three x, s and n directions may be variable in the curved contact surface. Attention is restricted here to prismatic or nearly prismatic solids, in which a constant x longitudinal direction may be defined in the neighbourhood of the contact. This happens in the vast majority of technically important rolling contact applications, in which the solids are essentially flat in rolling (x) direction around the contact. Relevant examples are the contacts of wheels on rails, and contacts in rolling bearings with curved races.

A difficulty that arises with curved contact surfaces concerns the determination of the applicable ICs, that are different for each particular geometry, and that are not exactly known *a priori*. The approach followed in Refs. [14,15] to obtain the necessary ICs was to calculate them numerically with FEM. An analytical approximation was proposed in Ref. [18] as an alternative, avoiding the work required for the numerical calculation. This is based on the surface orientations of points where loads are applied and displacements observed. However, this approximation brings some inaccuracies, some of which were pointed out in Ref. [19].

This work presents new ideas to improve the analytical approximation of the ICs for non-planar bodies. The limitations of the approximation are further assessed by comparison with numerically calculated ICs and by quantification of the consequent errors in the solution of conformal contact problems. To facilitate the identification of the different types of ICs involved, each of them is identified with an initial capital letter. *A* is used for the half-space ICs, *B* for the analytically approximated ICs of non-planar bodies, and *C* for the real (numerically calculated) ICs of non-planar bodies. The letter *I* is used for the generic designation of the different types of ICs. This notation is different from that used in Refs. [18,19], where *B* was used to reference both the half-space ICs and the approximated ones. Additional accents, numbers and letters are appended to the different ICs when necessary to associate them to particular bodies or geometries, or to identify different variants of them. Additionally, two subscripts i and j are used to specify the directions of the resulting displacement and the applied load respectively. Subscripts I and J indexing the corresponding elements are dropped in the sequel, for the sake of brevity.

3. Surface orientation-based approximation

3.1. Background

The aim is to get a simple way of approximating the ICs of non-planar solids, under the following assumptions:

- The surfaces are approximately prismatic (i.e. extruded in one direction) around the contact.

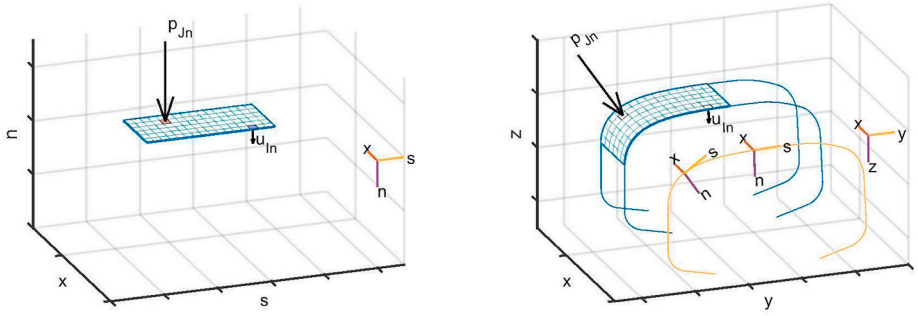

(a) Planar surface. (b) Curved surface.

Fig. 1. Surface discretization and influence coefficients in contact problems.

- The surfaces are smooth, not having local curvature radii small in relation to the contact patch dimensions.
- The distance between the contacting surfaces is small compared to the contact patch dimensions.
- The solids are massive (not hollow) around the contact. In this way, the load transmission beneath the contact surfaces resembles that of the half-space.
- The solids are homogeneous, isotropic, and with linear elastic behaviour.

These assumptions are usually fulfilled in relevant rolling contact applications, like in the wheel–rail case and in rolling bearings. A further restriction is set out in relation to the half-space-like local behaviour. This is that the contact should be far from surface borders or constraint locations as compared to contact patch dimensions. Satisfactory results have been obtained with the approximated ICs dealt with here in some initial tests in which this restriction was not fulfilled, but further work is necessary to determine the validity of this approach in such situations and assess the related errors.

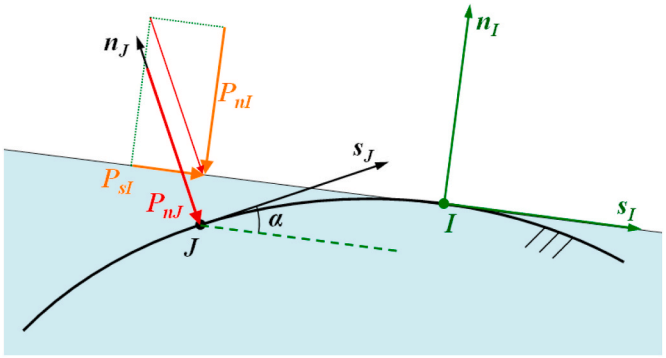

Fig. 2. Surface orientation-based B_{ij} approximation of ICs of non-planar solids. x direction perpendicular to the plane of the figure.

Fig. 2 depicts the basic idea behind the surface orientation-based calculation of the B_{ij} approximated ICs. Considering prismatic surfaces aligned in the x direction, a single rotation α around the x axis suffices to define the difference in surface orientation between different points.

To approximate the displacements at a surface point I due to a load applied at a point J, the load is decomposed into the x, s and n directions of the point I where the displacement is sought, and it is assumed that the contribution of the load component in each direction is equivalent to the corresponding one in the half-space. In other words, it is assumed that the behaviour of the solid is equivalent to a half-space tangent to its surface at I. The decomposition of a normal load acting on a convex surface is shown as an example in Fig. 2. According to this, a first approximation B of the ICs for non-planar solids is defined in Eq. (3).

$$\begin{bmatrix} B_{xx} & B_{xs} & B_{xn} \\ B_{sx} & B_{ss} & B_{sn} \\ B_{nx} & B_{ns} & B_{nn} \end{bmatrix} = \begin{bmatrix} A_{xx} & A_{xs} & A_{xn} \\ A_{sx} & A_{ss} & A_{sn} \\ A_{nx} & A_{ns} & A_{nn} \end{bmatrix} \cdot \begin{bmatrix} 1 & 0 & 0 \\ 0 & \cos(\alpha) & -\sin(\alpha) \\ 0 & \sin(\alpha) & \cos(\alpha) \end{bmatrix} = \begin{bmatrix} A_{xx} & A_{xs}c_\alpha + A_{xn}s_\alpha & A_{xn}c_\alpha - A_{xs}s_\alpha \\ A_{sx} & A_{ss}c_\alpha + A_{sn}s_\alpha & A_{sn}c_\alpha - A_{ss}s_\alpha \\ A_{nx} & A_{ns}c_\alpha + A_{nn}s_\alpha & A_{nn}c_\alpha - A_{ns}s_\alpha \end{bmatrix} \quad (3)$$
$$\text{Or, in compact form : } [B_{ij}] = [A_{ij}] \cdot [R_x(\alpha)]$$

The angle α in Eq. (3) is the difference in orientation between points I and J, and c_α and s_α stand for $\cos(\alpha)$ and $\sin(\alpha)$ respectively. The matrix $[R_x(\alpha)]$ is the rotation matrix related to the angle α. Eq. (3) may be interpreted as a rotation of the half-space ICs. The same reasoning and the same expressions may be applied to the combined ICs related to the displacement differences between two conforming contacting bodies (one of them convex and the other concave), choosing properly the sign of α in each case. Designating the upper body as the one in which the n axis points into, defining the displacement differences as the displacements of the upper body with respect to the lower, and considering positive stresses those applied on the upper body along the positive directions of the defined curvilinear coordinate system, α, measured from I to J, is positive counter-clockwise for the upper body while looking towards the negative x direction. The sign of α changes in the lower body.

3.2. Analogy with cylindrical ICs

The IFs of 2D cylindrical geometries subject to surface line loads are available in analytical form, and may be found in Ref. [21] for instance. The IFs for a cylindrical cavity are given in Eqs. (4) and (5) for normal and tangential loads N, T as depicted in Fig. 3. These IFs are designated with the a letter (in lower-case in order to distinguish from their corresponding ICs) as those of the half-space because they are exact

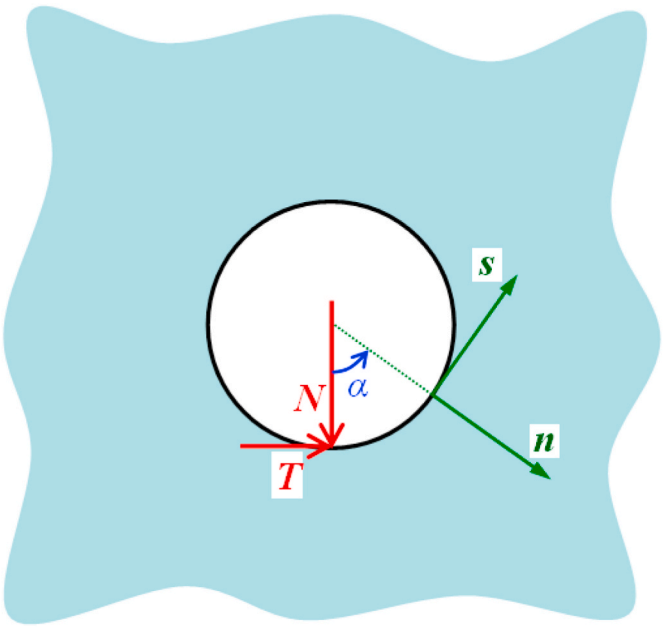

Fig. 3. Cylindrical cavity subject to surface line loads.

analytical.

$$a_{nn}^{cav} = a_{ss}^{cav} = \frac{1}{4\pi G}\left[(\kappa-1)\sin(\alpha)F(\tilde{\alpha}) - \left(\frac{\kappa+1}{2}\right)\cos(\alpha)\ln(2-2\cos(\alpha))\right] \quad (4)$$

$$a_{sn}^{cav} = -a_{ns}^{cav} = \frac{1}{4\pi G}\left[(\kappa-1)\cos(\alpha)F(\tilde{\alpha}) + \left(\frac{\kappa+1}{2}\right)\sin(\alpha)\ln(2-2\cos(\alpha))\right] \quad (5)$$

$$F(\tilde{\alpha}) = \frac{\tilde{\alpha} - \pi \times \mathrm{sgn}(\tilde{\alpha})}{2} \quad (6)$$

$$\tilde{\alpha} = \alpha - 2\pi\left\lfloor\frac{\alpha/\pi+1}{2}\right\rfloor \quad (7)$$

The superindex *cav* refers to the cavity. The function $F(\tilde{\alpha})$ is defined in Eq. (6), with angle $\tilde{\alpha}$ given in Eq. (7), as a function of the α angle depicted in Fig. 3. κ is Kolosov's constant, equal to $3-4\nu$ in plane strain, with ν the coefficient of Poisson, and G is the shear modulus. The IFs for the cylinder are similar, with some sign changes and additional rigid body displacements and rotations, depending on the loading and support conditions. The a_{ss} IF is equal to a_{nn}, as it happens with the half-plane. The minus sign between a_{sn} and a_{ns} in Eq. (5) comes directly from reciprocity.

The Flamant IFs of the half-plane [23] are denoted as a_{nn}^{hp} and a_{sn}^{hp} and are given in Eqs. (8) and (9). The same coordinates are used as for the cylindrical IFs above. The variable s_o in Eq. (9) is the necessary reference point in the s coordinate to define the origin of the normal displacements resulting from the normal line load, as in the half-plane the absolute magnitude of these is undetermined.

$$a_{nn}^{hp} = \frac{1-\nu}{\pi G}\ln\left|\frac{s_o}{s}\right| \quad (8)$$

$$a_{sn}^{hp} = -\mathrm{sgn}(\alpha)\frac{1-2\nu}{4G} \quad (9)$$

There is a similarity between the exact ICs of 2D cylindrical geometries and the B_{ij} approximation for 3D non-planar bodies. Comparing Eqs. (4) and (5) with Eq. (3), it can be seen that in both cases the ICs related to loads in the n and s directions are composed of a term multiplied by $\cos(\alpha)$ and another term multiplied by $\sin(\alpha)$. According to the B_{ij} approximation, the term $-\frac{1}{4\pi G}\left(\frac{\kappa+1}{2}\right)\ln(2-2\cos(\alpha))$ would be assimilated to a_{nn}^{hp} of the half-plane, and the term $\frac{1}{4\pi G}(\kappa-1)F(\tilde{\alpha})$ to a_{sn}^{hp}. Indeed, it may be verified that these terms in Eqs. (4) and (5) converge towards the corresponding IFs of the half-plane for small α angles, according to Eqs. (10) and (11).

$$-\frac{\kappa+1}{8\pi G}\lim_{\alpha\to 0}(\ln(2-2\cos(\alpha))) = \frac{1-\nu}{2\pi G}\times 2\ln\left(\frac{1}{\alpha}\right) \propto a_{nn}^{hp} \quad (10)$$

$$\frac{\kappa-1}{4\pi G}\lim_{\alpha\to 0}F(\tilde{\alpha}) = -\mathrm{sgn}(\alpha)\frac{1-2\nu}{4G} = a_{sn}^{hp} \quad (11)$$

Eq. (10) uses a series expansion of the cos function that is truncated after the $\alpha^2/2$ term, i.e. $\cos(\alpha) \approx 1-\alpha^2/2$, neglecting higher order terms for $\alpha\to 0$. The proportionality symbol $\propto$ is used instead of the equality, indicating "similar asymptotic behaviour" because the absolute magnitude of the half-plane a_{nn}^{hp} IF is undetermined as mentioned before.

A difference between the B_{ij} approximation and the exact ICs for cylindrical geometries is found in a factor variable with α present in the term $\frac{1}{4\pi G}(\kappa-1)F(\tilde{\alpha})$ in Eqs. (4) and (5), equal to $|\pi-|\alpha||/\pi$. It has been tried to include this factor in the A_{sn} half-space ICs for use in the B_{ij} ICs, so as to make them more similar to the exact ICs for cylindrical geometries, but it has not been found any consistent precision improvement of the B_{ij} ICs for 3D prismatic solids. Moreover, if the materials of the two contacting bodies are elastically similar, as in the wheel–rail application, the combined half-space A_{sn} are zero, and in this case the factor $|\pi-|\alpha||/\pi$ becomes irrelevant for the B_{ij} approximation of the combined ICs.

3.3. Moving the tangent point of the equivalent half-space

A variant of the approach of Section 3.1 is obtained by considering a tangent plane at the location J where the load is applied as illustrated in Fig. 4.

This gives approximated ICs denoted by $\overline{B}_{ij}$ cf. Eq. (12).

$$\left[\overline{B}_{ij}\right] = [R_x(\alpha)]\cdot[A_{ij}] = \begin{bmatrix} A_{xx} & A_{xs} & A_{xn} \\ A_{sx}c_\alpha - A_{nx}s_\alpha & A_{ss}c_\alpha - A_{ns}s_\alpha & A_{sn}c_\alpha - A_{nn}s_\alpha \\ A_{sx}s_\alpha + A_{nx}c_\alpha & A_{ss}s_\alpha + A_{ns}c_\alpha & A_{sn}s_\alpha + A_{nn}c_\alpha \end{bmatrix} \quad (12)$$

A third variant $\widehat{B}_{ij}$ is set out imagining the tangent half-space halfway between points I and J, oriented at an angle $\beta = \alpha/2$ apart from the tangents at those points. This could be thought of as a mix between the previous B_{ij} and $\overline{B}_{ij}$ variants. Defining $A_{s+n} = (A_{ss}+A_{nn})/2$, and $A_{s-n} =$

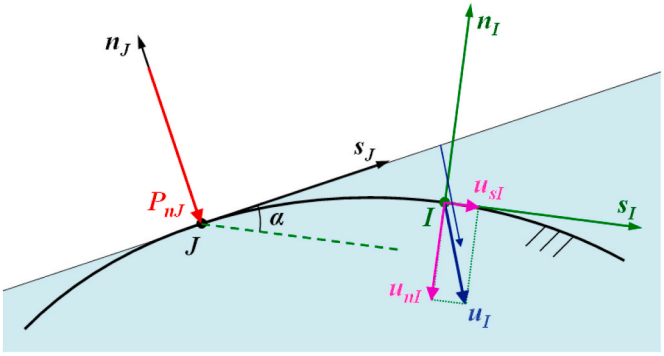

Fig. 4. $\overline{B}_{ij}$ variant of surface orientation-based approximated ICs.

$(A_{ss} - A_{nn})/2$, the resulting expressions for the $\widehat{B}_{ij}$ ICs are given in Eq. (13).

$$\left[\widehat{B}_{ij}\right] = [R_x(\beta)]\cdot[A_{ij}]\cdot[R_x(\beta)] = \begin{bmatrix} A_{xx} & A_{xs}c_\beta + A_{xn}s_\beta & -A_{xs}s_\beta + A_{xn}c_\beta \\ A_{xs}c_\beta + A_{xn}s_\beta & A_{s+n}c_\alpha + A_{s-n} + A_{sn}s_\alpha & -A_{s+n}s_\alpha + A_{sn}c_\alpha \\ A_{xs}s_\beta - A_{xn}c_\beta & A_{s+n}s_\alpha - A_{sn}c_\alpha & A_{s+n}c_\alpha - A_{s-n} + A_{sn}s_\alpha \end{bmatrix} \tag{13}$$

The $\widehat{B}_{ij}$ ICs have the merit of preserving the symmetries $\widehat{B}_{sx} = \widehat{B}_{xs}$, $\widehat{B}_{xn} = -\widehat{B}_{nx}$ and $\widehat{B}_{sn} = -\widehat{B}_{ns}$; and hence verifying reciprocity.

In the remainder, the B_{ij} and $\widehat{B}_{ij}$ variants will be considered. The notation B will be used generically also, designating any of the variants of ICs presented here as well as the extension of the following section.

4. Extension of approximated ICs for the geometric differential stiffness

The load/displacement decomposition effect, which is the basis of the surface orientation approach for the calculation of the B_{ij} ICs, explains many of the differences between the ICs of non-planar solids and those of the half-space, but there are other differences which are not explained by this effect. In Ref. [19], clear discrepancies were pointed out between the combined B_{xn} and C_{xn} ICs of two conforming bodies with elastically similar materials.

These discrepancies are attributed to the difference between the stiffnesses of the convex and concave conforming bodies, that comes as a result of the different geometry of their cross sections: the concave body, which has more material, tends to be stiffer than the convex one. This characteristic is not captured by the B_{ij} ICs treated in Section 3. This section provides an extension for the B_{ij} to overcome this limitation. For most of the ICs, the effect of the surface orientation proves to be dominant in the deviation of the ICs of non-planar solids from those of the half-space, and the B_{ij} previously presented provide a good approximation. However in the particular case of the C_{xn} the effect of the geometric differential stiffness between the two conforming bodies plays a more important role. Consequently that approximation is not satisfactory for the C_{xn}, and it becomes necessary to take into account the effect of the geometric differential stiffness to improve it.

The approach followed here to incorporate the differential stiffness effect is to define modified, effective elastic properties of the conforming bodies, that vary as a function of the distance from the loaded element in the surface. Close to the loaded element, at a distance much lower than the typical dimensions of the general features of the cross sections of the bodies, the bodies look like half-spaces, their geometric differential stiffness tends to zero, and hence their effective elastic properties will be their real ones. As the distance increases, a bigger portion of the material and (unequal) cross sections of the bodies influences their behaviour, and more difference between their stiffnesses will be noted. Their approximated ICs are then calculated with modified elastic properties instead of the real ones of the bodies to approximate the variation of the geometric differential stiffness between the conforming bodies.

The modified, effective elastic properties of the bodies vary between their real values at zero distance from the loaded element, to some limit values at a given limit distance from the loaded element related to the geometry of the cross sections of the bodies. This is represented here using the function defined in Eq. (14). This form of empirical equation has been chosen with the aim of providing a continuous transition in space for the values of the effective elastic properties, having the possibility of adjusting the rate of change at both limits of the variation interval.

$$f(r) = f^0 + \left(f^\infty - f^0\right) \times \left[(1-\rho)\cdot\rho^{m_f} + \rho\cdot(1-(1-\rho)^{n_f})\right] \tag{14}$$

$$r = \sqrt{x_r^2 + s_r^2},\ \rho = \min\left(1, r \,/\, r_{\infty f}\right). \tag{15}$$

The nomenclature used in Eq. (14) is as follows: f refers to an elastic property, such as the combined G, ν or K of both bodies, or an individual elastic constant of one of the bodies. For each property, f^0 is its effective value at zero distance from the centre of the loaded element, equal to its real value, and f^∞ its effective value at infinite distance from the loaded element. (x_r, s_r) is a position from the centre of the loaded element in x and s directions, r the actual surface distance from the centre of the loaded element as defined in Eq. (15), and $r_{\infty f}$ a limit distance beyond which the elastic property f no longer changes and is equal to its

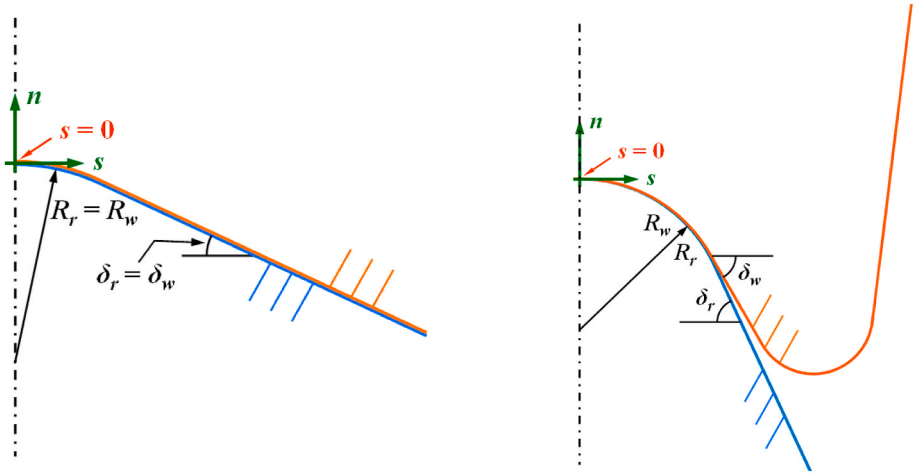

(a) Geometry 1. (b) Geometry 2.

Fig. 5. Cross sections of conforming bodies, symmetric about $s = 0$, with elastically similar materials.

effective value at infinity f^{∞}. m_f and n_f are two constant exponents for each elastic property f. The effective elastic properties obtained with Eq. (14) are used to calculate modified A_{ij}, designated as A'_{ij}. These A'_{ij} are then used in Eq. (13) for the $\widehat{B}$ ICs presented in Section 3. This extended version of the $\widehat{B}_{ij}$ is designated as $\widehat{B}'$.

An empirical approach is followed to determine the parameters f^{∞}, $r_{\infty f}$, m_f and n_f for each elastic property. The C ICs are calculated numerically with FEM for a single lateral position of the load in the cross sections of the contacting bodies, and these are used as a reference to adjust the parameters in Eq. (14). A drawback is that numerical calculation of some of the C_{ij} is involved, but this is less costly than computing the full C_{ij} matrices. The lateral position used for the loaded element is chosen in the central zone of the expected contact patches.

With the $\widehat{B}'_{ij}$ ICs, it is aimed specifically at improving the approximation of the C_{xn}, where the differential stiffness effects are more prominent. Taking this into account, here the $\widehat{B}'_{ij}$ will be computed on the basis of adjusting just the elastic mismatch constant of both bodies K, seeking to improve the approximation for the C_{xn} while affecting the other B_{ij} as little as possible. Thus, the $\widehat{B}_{xn}$ and the $\widehat{B}_{sn}$ will be affected most by this extension, as well as their reciprocals, and to a lesser extent the $\widehat{B}_{xs}$, $\widehat{B}_{ss}$ and the $\widehat{B}_{nn}$ through the contributions of the A'_{xn} and A'_{sn}.

5. Comparison of approximated and numerically calculated ICs

5.1. Description of the test-cases

Two geometries are considered for comparison between the different I_{ij} ICs, $I \in \{A,B,\widehat{B},\widehat{B}',C\}$, with cross sections depicted in Fig. 5 and related parameters listed in Table 1. The materials of the conforming bodies are elastically similar in both cases. Two prismatic bodies are considered in geometry 1, and a concave wheel on a convex rail in geometry two. In both geometries the lower convex body is designated as the rail, and the upper concave one as the wheel. Both geometries have a cross section with circular central zone delimited by inclined straight sections, with different subtended angles in each case. Besides testing the performance of the B_{ij} in each of these cases, the comparison of their respective C_{ij} allows to appreciate the effect of their different geometries. An objective is to observe the effect of the different overall cross sections of each geometry (with different inclinations of the side straight parts) on the ICs in the central circular zone, common in both geometries. This serves as a test for the consistency of the surface orientation based approach, which takes into account specifically surface orientation differences in the region of interest.

Table 1
Parameters of conforming bodies considered for the study of ICs.

Symbol	Description	Units	Geometry no.	
			1	2
δ_r	Surface inclination of rail (lower body)	deg	25.5	65
δ_w	Surface inclination of wheel (upper body)	deg	25.5	60
R_r	Radius of circular part of cross section of rail	mm	10.0	10.0
R_w	Radius of circular part of cross section of wheel	mm	10.0	10.1
R_{roll}	Nominal rolling radius of wheel (at $s = 0$)	mm	∞	500
E	Young's Modulus	GPa	210	210
ν	Coefficient of Poisson	–	0.28	0.30
a	Longitudinal half-side of loaded element	mm	0.200	0.167
b	Lateral half-side of loaded element	mm	0.200	0.158

Comparisons are made for the combined ICs of two bodies together, as well as for the individual ones for each of the bodies of geometry 2. The geometries are identified with superindex 1 for the geometry of Fig. 5a and 2 for the geometry of Fig. 5b. On the other hand, for the individual ICs of each of the bodies of geometry 2 superindex "2,*r*" is used for the rail and "2,*w*" for the wheel. Some of the ICs are omitted for clarity in some graphs of this section, when they are equivalent or very similar to others shown.

The ICs are considered for a uniformly loaded rectangular element of the surface, centred in the lateral symmetry plane of the bodies (i.e. at $s = 0$), and aligned with the x and s directions, with different dimensions in each case as indicated in Table 1. The ICs are given for a unit total load rather than for a unit pressure in each loaded element, to compare directly the ICs of both geometries, and are normalized additionally with E and R_r. As listed in the table, slightly different values of ν have been considered for each of the geometries. This difference does not have significant effects in the comparisons shown here.

The C_{ij} have been calculated with FE models for both geometries shown in Fig. 5. The FE mesh has been refined locally around the loaded element for geometry 1, to provide adequate resolution for the step load variation and capture the relatively high displacement gradients. This local mesh refinement has been omitted for the C_{ij} corresponding to geometry 2. Instead, extrapolation is used on the basis of the trends for the half-space for the displacements in the loaded element and its neighbouring elements. This is justified because the loaded element is much smaller than the typical dimensions of the cross section considered, such that the solids can be regarded as flat, similar to half-spaces, around the loaded element. A detailed study on the effects of mesh characteristics and precision of the numerically calculated ICs is

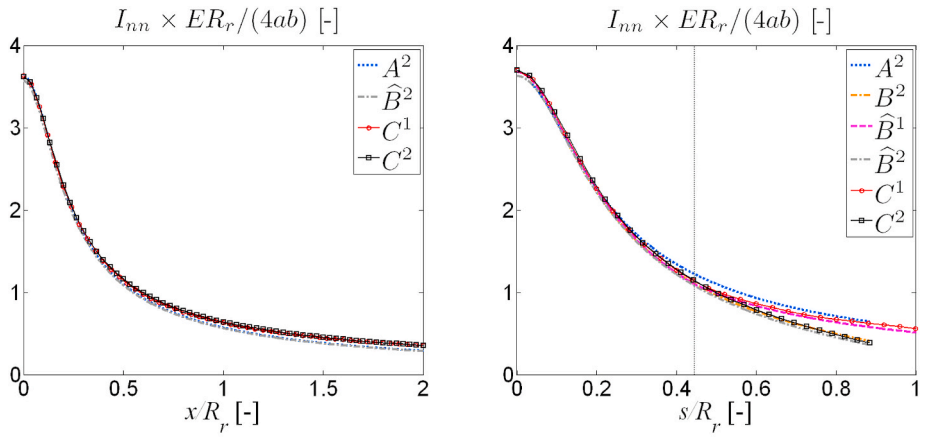

(a) Along x at $s/R = 0.16$. (b) Along s at $x/R = 0.16$.

Fig. 6. A_{nn}, B_{nn} and C_{nn} combined ICs for geometries 1 and 2 of Fig. 5.

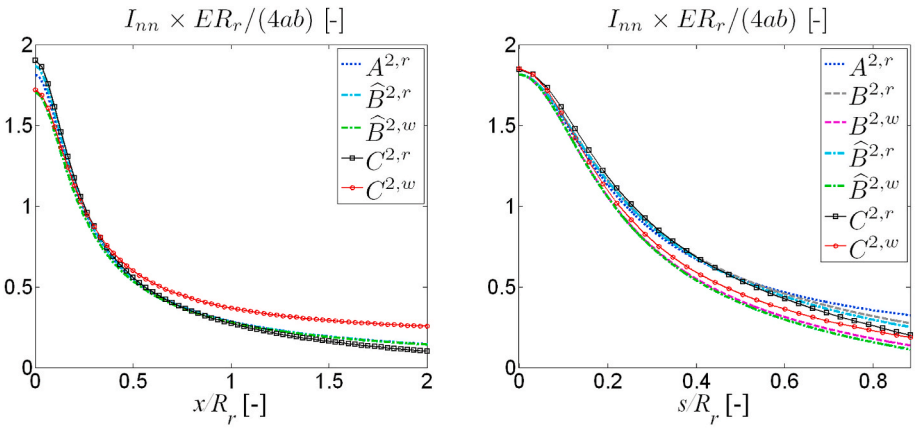

(a) Along x at $s/R = 0.16$. (b) Along s at $x/R = 0.16$.

Fig. 7. A_{nn}, B_{nn} and C_{nn} individual ICs for geometry 2 of Fig. 5.

presented in Ref. [20].

Appropriate global displacements are discounted from the C_{ij} in each case for an adequate comparison of the C_{ij} with the rest of ICs. A global displacement is applicable for each load case with stress applied in $j = n$, x, or s direction, in the same direction as the applied load, $i = j$, taking into account the geometric and load symmetry. These global displacements are calculated so that the direct C_{ii} IC is made equal to the A_{ii} three elements away from the loaded element in the longitudinal direction. The displacements would ideally be matched at the loaded element itself, but this is hampered by numerical errors contained in the FE solutions (mostly for geometry 2, where no local mesh refinement around the loaded element is employed). A three-element distance is used as a compromise between big enough to reduce numerical errors to an acceptable level and yet small enough so that the variations of the C_{ij} and A_{ij} may still be assumed equivalent. Additionally, a global rotation is considered around the x axis for the load case with lateral tangential traction, calculated so that the vertical displacements at points symmetrically located in the lateral direction at either side of the loaded element, at its same longitudinal position, and far from it are made equal. This global rotation is mostly produced in the convex body, which tends to globally bend under a lateral load. It is much lower for geometry 1 than for geometry 2, owing to the lower surface inclination δ_r of the convex section.

In the following, Section 5.2 examines the direct I_{ii}'s and tangential I_{xs}, while Section 5.3 discusses the tangential to normal ICs I_{xn} and I_{sn}. The deviations of the ICs of convex bodies on the one hand and of concave bodies on the other, with respect to the corresponding half-space ICs, are generally opposite to each other. These deviations counteract each other in the combined ICs of the two conforming bodies in the case of the I_{ii} and I_{xs} ICs, and are added together in the case of the I_{xn} and I_{sn} ICs.

5.2. Comparison of I_{ii}'s and I_{xs}

Figs. 6–10 show the ICs with subindices *nn*, *ss* and *xs*, in non-dimensional section distances from the centre of the loaded element, x/R_r and s/R_r, along sections passing at 1.6 mm from the centre of the loaded element. This offset is used to avoid the relatively high displacements at the singular loaded element masking the variations of the ICs outside it. Besides, the trends of the ICs close to the loaded element converge to those of the half-space.

For geometry 1, the limit between the circular and straight sections is marked with a vertical dotted line in the graphs along the lateral direction s. This change in geometry has an appreciable effect on the trends of several of the ICs as may be appreciated in the different graphs.

The curves of the direct I_{ii}'s are symmetric about $(x, s) = (0, 0)$ in longitudinal and lateral directions, while those for I_{xs} are skew symmetric.

The highest deviations between the combined C_{nn} and the A_{nn} occur in the lateral direction, as may be seen in Fig. 6. Both the combined (Fig. 6) and the individual C_{nn} (Fig. 7) tend to become smaller than the corresponding A_{nn} as the difference in orientation α from the point of

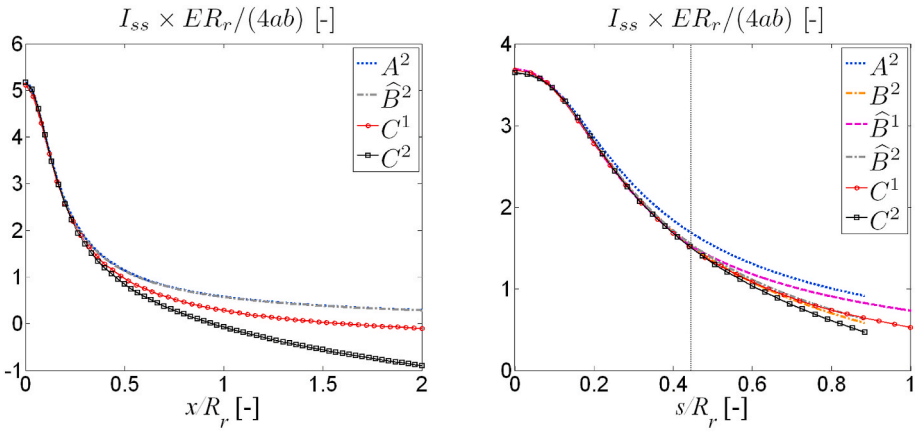

(a) Along x at $s/R = 0.16$. (b) Along s at $x/R = 0.16$.

Fig. 8. A_{ss}, B_{ss} and C_{ss} combined ICs for geometries 1 and 2 of Fig. 5.

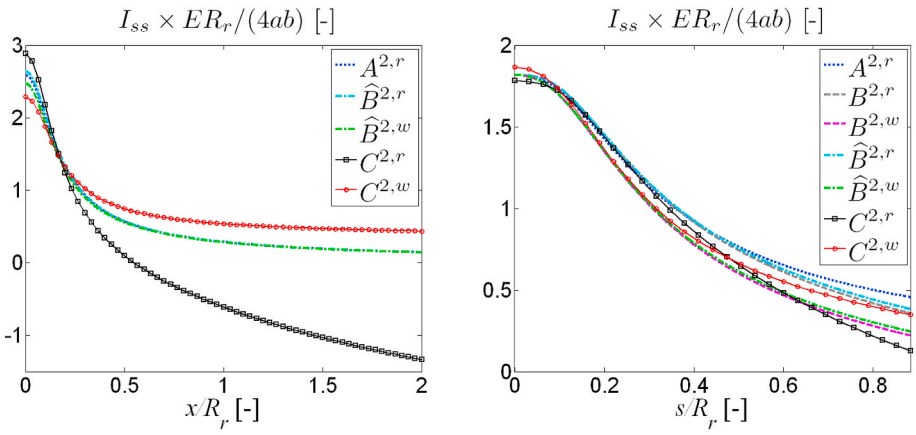

(a) Along x at $s/R = 0.16$. (b) Along s at $x/R = 0.16$.

Fig. 9. A_{ss}, B_{ss} and C_{ss} individual ICs for geometry 2 of Fig. 5.

load application increases, particularly in the case of the combined C_{nn}, and in the individual ones of the concave body. The B_{nn} capture these deviations well in both geometries considered, as shown in Fig. 6b and Fig. 7b. The deviations between the individual C_{nn} and A_{nn} of the convex body are smaller, as may be seen in Fig. 7b. This is again well represented by either the B_{nn} or the $\widehat{B}_{nn}$. Referring to Eq. (3), the second term in the equation for B_{nn} is positive in the case of the convex body (including its minus sign), and opposes the decrease of the first and principal term with respect to A_{nn}. The different cross sections of both geometries do not produce big differences in the variations of the combined I_{nn} in the longitudinal direction, as seen in Fig. 6a. The most notable differences in this direction occur in the individual I_{nn} of the concave body as seen in Fig. 7a, with the $C_{nn}^{2,w}$ having less pronounced variations than either the corresponding A or B ICs.

The combined C_{ss}, Fig. 8, have significant deviations with respect to the A_{ss} in both principal directions of the surface, tending to become smaller as the distance with respect to the loaded element increases. The trend in the lateral direction is relatively well reproduced with the B_{ss} (Fig. 8b), but not in longitudinal direction (Fig. 8a). The C_{ss} maintain a considerably higher gradient than the B_{ss} as the longitudinal distance from the loaded element increases, especially for geometry 2, with the highest difference between the convex and the concave cross sections. This is attributed to the twist of the convex body under lateral load, which causes sections away from the loaded one to be more uncoupled from it than in the case of the half-space. The deviations between the individual C_{ss} and both the corresponding A and B ICs are considerably higher, cf. Fig. 9, especially for the convex body in the longitudinal direction, as can be seen in Fig. 9a. The deviations with respect to the A_{ss} are of opposite sign in each of the bodies, and tend to oppose each other in the combined C_{ss}.

The deviations observed between the individual C_{xx} and A_{xx}, not shown here, are of similar nature, but of smaller magnitude. Additionally, their differences are more compensated, in such a way that in the cases considered here with elastically similar materials, they turn out to nearly cancel each other. As a result, the differences between the combined A_{xx} and C_{xx} are very small in longitudinal as well as lateral directions, and the combined C_{xx} are highly similar between the two geometries considered. The surface orientation-based approximation, that amounts to the equality of B_{xx} and A_{xx}, works well for the combined C_{xx} of both solids. This shows how differences between the C_{ij} and A_{ij} for the convex and concave individual bodies may be compensated in the combined C_{ij} and A_{ij}. However, the extent of this compensation depends on the relative stiffnesses of the two bodies. This observation is also applicable for the I_{nn}, I_{ss} and I_{xs} ICs.

For the tangential cross ICs I_{xs}, shown in Fig. 10, the highest differences between the C_{xs} and both the A_{xs} and the B_{xs} happen in the lateral direction (Fig. 10b). These are attributed to the difference in longitudinal stiffness of the two bodies, resulting from the cross sections. The individual C_{xs} of the convex body deviate more from the half-space A_{xs} than those of the concave body. This indicates that the material missing in the convex cross section (with respect to the half-space), has a greater effect than the additional material present in the concave section, like

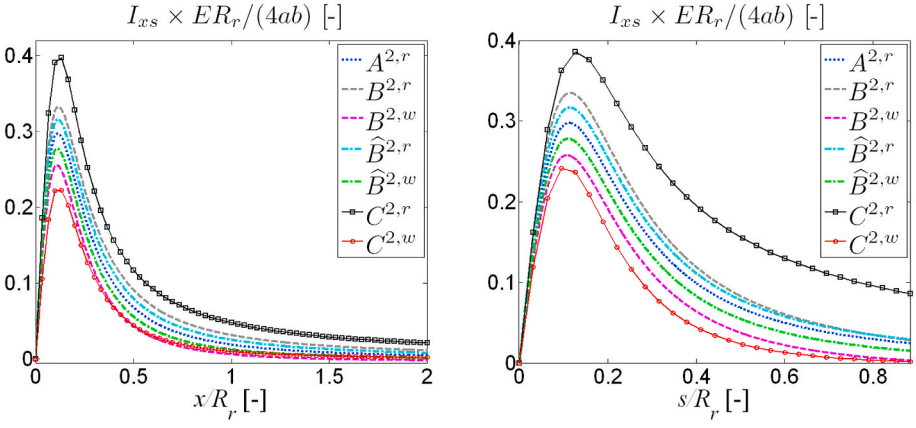

(a) Along x at $s/R = 0.16$. (b) Along s at $x/R = 0.16$.

Fig. 10. A_{xs}, B_{xs} and C_{xs} individual ICs for geometry 2 of Fig. 5.

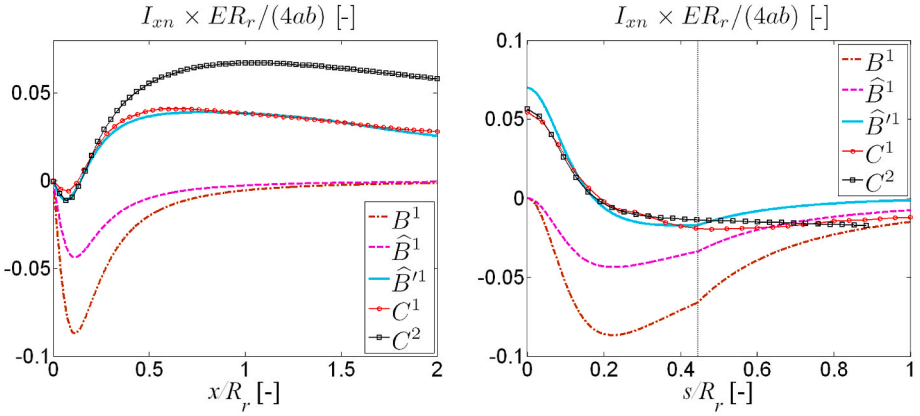

(a) Along x at $s/R = 0.16$. (b) Along s at $x/R = 0.16$.

Fig. 11. A_{xn}, B_{xn} and C_{xn} combined ICs for geometry 1 of Fig. 5.

Table 2
Parameters of adjusted effective elastic property K for both geometries.

	Geometry 1	Geometry 2
K^∞	−0.065	−0.145
$r_{\infty,K}/R_r$	1.60	2.25
m_k	0.67	0.90
n_k	1.80	2.00

with the C_{ss}. The B_{xs} and $\widehat{B}_{xs}$ capture only part of the differences between the A_{xs} and C_{xs}, with B_{xs} performing better in this case than $\widehat{B}_{xs}$. The performance of the B_{xs}'s is not fully satisfactory. The consequences of this are limited because the magnitude of the I_{xs} is significantly smaller than that of the direct I_{xx} and I_{ss} ICs.

5.3. Comparison of I_{xn} and I_{sn}

This section examines the I_{xn} and the I_{sn} ICs. The curves passing at a distance of 1.6 mm from the centre of the loaded element are considered, as with the ICs examined in Section 5.2. The curves of the I_{xn} are skew-symmetric in x and symmetric in s, and the curves of the I_{sn} are symmetric in x and skew-symmetric in s at $(x, s) = (0, 0)$. While these ICs have also a considerably lower magnitude than the direct I_{ii} ICs, their influence can be significant in the tangential contact problem as shown in previous works [18,19]. This is because the normal pressures usually reach much higher values than the tangential tractions. Comparisons with the $\widehat{B}'$ ICs introduced in Section 4 are included for the combined ICs.

The combined I_{xn} are plotted in Fig. 11 for geometry 1 and in Fig. 12 for geometry 2. The C_{xn} of both geometries are included in both figures to better appreciate the differences between them. The parameters for the effective elastic property K are listed in Table 2 (cf. Eq. (14)) as used for the combined $\widehat{B}'_{xn}$ shown in these figures.

As expected, the differential stiffness effect is stronger in geometry 2, and consequently its C_{xn} reach higher values than the C_{xn} of geometry 1. This is seen in the plots along x (Fig. 11a and Fig. 12a). The B_{xn} prove to be a poor approximation for both geometries. Upon examination of the individual I_{xn} in Fig. 13, it may be noted that the B_{xn} and the $\widehat{B}_{xn}$ predict the highest displacements in the concave body, while the highest individual C_{xn} (in magnitude) are those of the convex body. Fig. 13a shows that the highest deviations between individual C_{xn} and other I_{xn} occur in the convex body. The adjusted $\widehat{B}'_{xn}$ provide a much better approximation of the combined C_{xn}, especially along x, although the values are somewhat overestimated close to the loaded element. This happens mostly for geometry 1, as shown in Fig. 14 along $s = 0$ (i.e. at the same lateral position as the loaded element).

Part of the differences between the C_{xn} of both geometries may be attributed to the difference in the longitudinal curvature of the upper bodies, using a prismatic body in geometry 1 and a body of revolution in geometry 2. The influence of the longitudinal curvature on these ICs may be estimated using the change in surface orientation in longitudinal

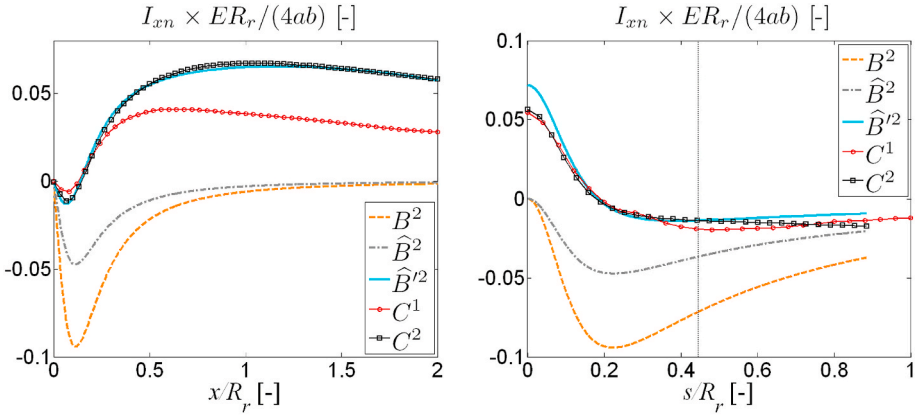

(a) Along x at $s/R = 0.16$. (b) Along s at $x/R = 0.16$.

Fig. 12. A_{xn}, B_{xn} and C_{xn} combined ICs for geometry 2 of Fig. 5.

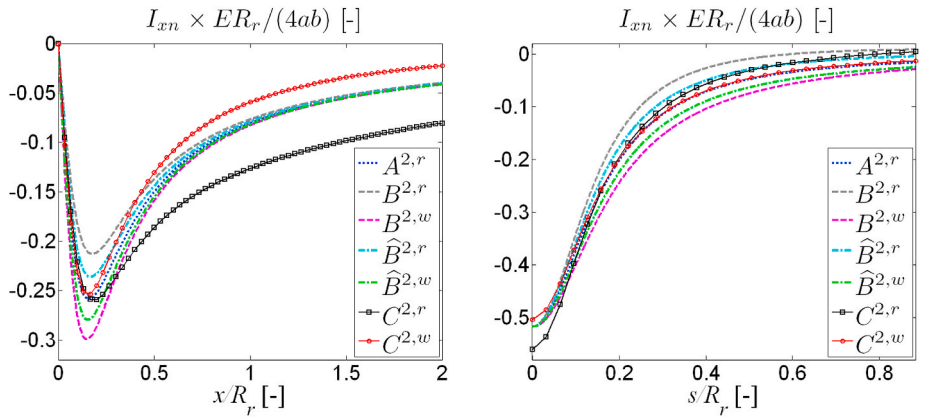

(a) Along x at $s/R = 0.16$. (b) Along s at $x/R = 0.16$.

Fig. 13. A_{xn}, B_{xn} and C_{xn} individual ICs for geometry 2 of Fig. 5.

direction, extending the $\widehat{B}_{xn}$ approximation. Doing this, specifically the $\widehat{B}_{xn}$ at the same lateral position than the loaded element (i.e. with $\alpha = 0$) would be computed as indicated in Eq. (16). This is obtained exchanging the s and x coordinates in the formula for $\widehat{B}_{sn}$ in Eq. (13). In this equation, $A^w_{x+n} = (A^w_{xx} + A^w_{nn})/2$, A^w_{xx} and A^w_{nn} are individual ICs of the wheel, and α_x is the angular difference in the wheel surface orientation in longitudinal direction (analogous to α in the lateral direction).

$$\widehat{B}_{xn} \approx A_{xn}\cos(\alpha_x) - A^w_{x+n}\sin(\alpha_x) \tag{16}$$

The first term is not altered by longitudinal curvature, as $x \ll R_{roll}$, $\cos(\alpha_x) \approx 1$ in practical contact problems. The influence of longitudinal curvature on C_{xn} therefore comes from the second term. In Fig. 14, this term is discounted from the combined C_{xn} computed for geometry 2 as shown by the curve labelled as "$C^2 + A^{2,w}_{x+n}\sin(\alpha_x)$". This way, this curve is an estimate of the C_{xn} that would be computed for geometry 2 if both bodies were prismatic. Since $A^{2,w}_{x+n}$ is approximately proportional to $1/x$ outside the loaded element and $\sin(\alpha_x) \approx \alpha_x \approx x/R_{roll}$, the second term in the right hand side of Eq. (16) is approximately constant in x and proportional to the longitudinal curvature. As may be seen in Fig. 14, the

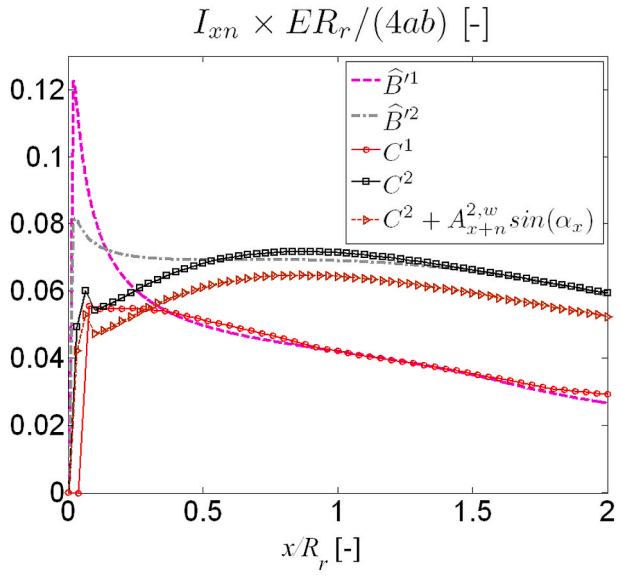

Fig. 14. A_{xn}, B_{xn} and C_{xn} combined ICs for geometries 1 and 2 of Fig. 5, along x at $s = 0$.

estimated effect of the longitudinal curvature of the wheel on the C_{xn} computed for geometry 2 explains part of the differences between the C_{xn} computed for both geometries. However, this effect is small compared to the remaining differences between the C_{xn} of each geometry, attributed to the different magnitude of the geometric differential stiffness in each case.

The most notable differences between the A_{ij} and C_{ij} crossed ICs (with $i \neq j$) occur in the I_{sn}. These are examined in Fig. 15 and Fig. 16. As it happens with the a_{sn} of cylindrical geometries (cf. Eq. (5) for the cylindrical cavity), the individual C_{sn} of the convex body are considerably lower than those of the half-space in the vicinity of the loaded zone, and the C_{sn} of the concave body are higher in magnitude, cf. Fig. 16. Another example of a non-planar solid with known IFs is the elastic sphere [24, 25], with this same behaviour. As with the I_{xn}, the differences between the individual A_{sn} and C_{sn} of the two solids are added in the combined ICs instead of compensated with each other.

The C_{sn} are adequately captured with both the B_{sn} and the $\widehat{B}_{sn}$, for the combined (Fig. 15) as well as for the individual (Fig. 16) I_{sn} of each body, especially inside the circular zone of the cross sections. The greatest discrepancies are seen in the lateral trends beyond the change from circular to straight profile in geometry 1. The B_{sn} approximate better the C_{sn} than the $\widehat{B}_{sn}$ in both geometries considered, and the approximation of the $\widehat{B}'_{sn}$ is worse than that of the $\widehat{B}_{sn}$.

A considerable part of the differences between the C_{sn} on the one hand, and $\widehat{B}_{sn}$ and $\widehat{B}'_{sn}$ on the other, turns out to amount to a rigid body vertical displacement. This does not affect the solution of contact problems except for the relative displacement of the bodies at a given load. This is shown with the C^* curves in Fig. 15, that are obtained by adjusting the global vertical displacements discounted to the C_{sn} to match better with the $\widehat{B}'_{sn}$. On the other hand, differences between different I_{sn} give rise to considerable differences in some of the results in the tangential part of the contact problem, as shown in Section 6.2.

It has been seen that the approximated ICs have different accuracies for each type of IC. Also, the accuracy of the approximated ICs depends among others on the shape of the non-planar surfaces; the affection of the sudden curvature change in the cross section of geometry 1 on the accuracy of the B_{sn} beyond the lateral position of this change is an example of this. Overall, it may be concluded that the surface orientation-based approximation gives a good first order estimation of the main deviations between the ICs of non-planar solids and those of the half-space. Additionally, with a simple reasoning it provides insight into the way in which these deviations occur. However, some limitations of the approximation are apparent, and additional work is needed to overcome them.

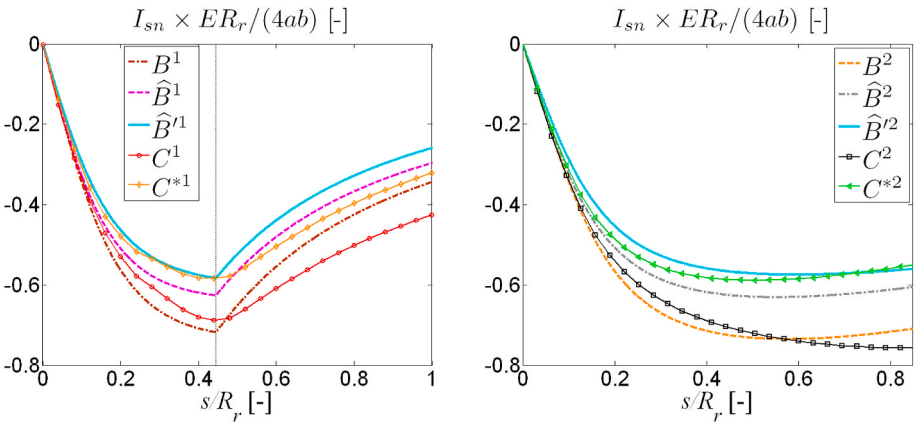

(a) Geometry 1. (b) Geometry 2.

Fig. 15. A_{sn}, B_{sn} and C_{sn} combined ICs for geometries 1 and 2 of Fig. 5 along s at $x/R = 0.16$.

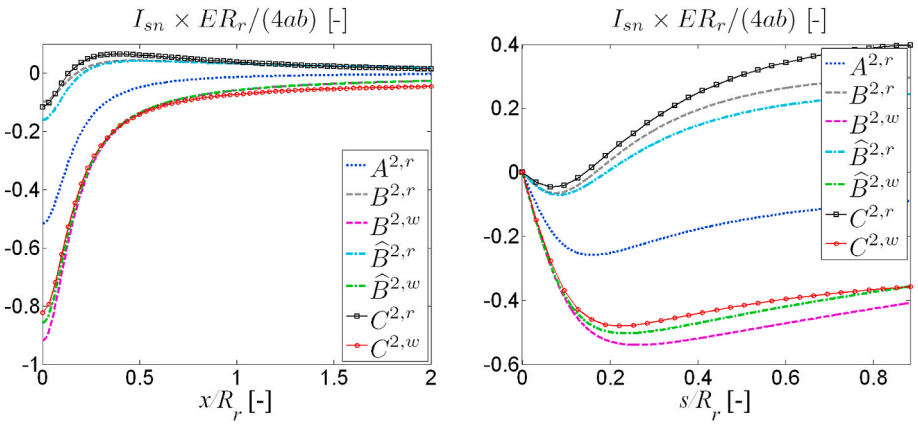

(a) Along x at $s/R = 0.16$. (b) Along s at $x/R = 0.16$.

Fig. 16. A_{sn}, B_{sn} and C_{sn} individual ICs for geometry 2 of Fig. 5.

6. Performance of approximated ICs in the solution of conformal contact problems

Here numerical computations are reported for different wheel–rail conformal contact test cases, assessing the performance of the different variants of approximated ICs in the normal and the tangential parts of the contact problem. A version of the exact contact theory with capacity to solve conformal contact problems is used for this purpose, named CECT [18,19]. Each test case is solved with different sets of ICs, to evaluate to which extent errors in the ICs affect contact related outputs.

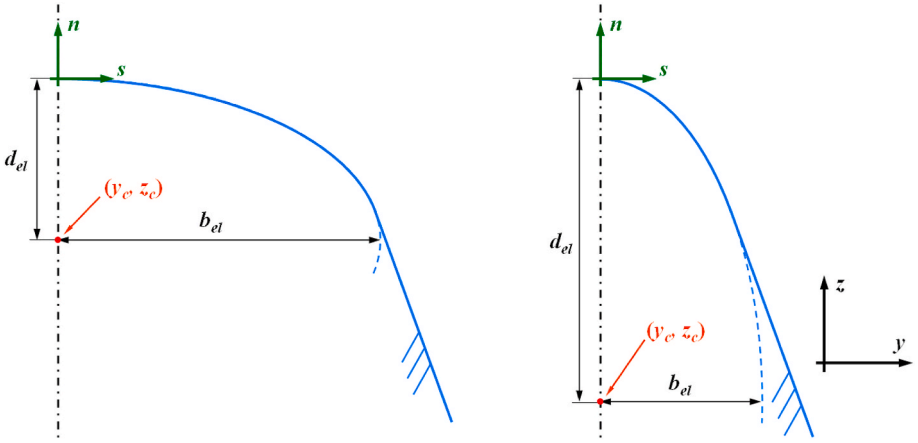

(a) Test case “wide”. (b) Test case “tall”.

Fig. 17. Rail cross sections with elliptical central zone.

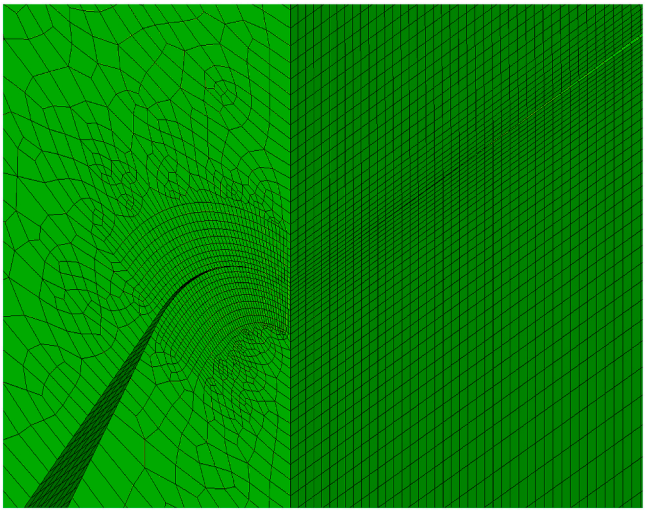

Fig. 18. FE mesh detail for test case "tall". Isometric view of cut at contact centre along longitudinal and lateral directions.

For the normal part of the contact problem, presented in Section 6.1, additional reference results are shown obtained with FEM contact analyses. Refined meshes have been used in these computations, in order to avoid the errors associated to the mesh resolution being significant in relation to the differences between the different sets of ICs. The contact calculations with CECT have been performed with meshes encompassing about 50 elements inside the contact in the lateral direction, and 40 in the longitudinal, except for the compression cases at lower loads. The FEM contact models have been constructed with finer meshes.

6.1. Normal contact

This section evaluates the errors made in the solution of the normal part of the contact problem when using approximated ICs in cases of conformal contact between bodies with different cross sections. The precision of the A_{nn} and the B_{nn} was studied before in Ref. [19] for conforming bodies with circular geometry in their cross sections. This is extended here to bodies with different non-circular cross sections, to assess the importance of the form of the contact angle variation across s. Additionally, the $\widehat{B}_{nn}$ are included in the comparison.

Description of geometries used . Two test cases are considered, with a concave wheel placed on a convex rail aligned in longitudinal direction, x, with zero yaw angle and mean contact angle. Therefore the geometries are symmetric along the overall longitudinal and lateral directions at the central point of the contact at $(x,s) = (0,0)$.

In each test case the bodies have different elliptical cross sections in the vertical plane perpendicular to x. The geometries are defined with the semi-axes b_{el} and d_{el} of their elliptical cross sections in the overall lateral and vertical directions, respectively, i.e.

$$\left(\frac{y-y_c}{b_{el}}\right)^2+\left(\frac{z-z_c}{d_{el}}\right)^2=1,\ \text{or}\ y=y_c+b_{el}\cos(\theta), z=z_c+d_{el}\sin(\theta). \tag{17}$$

The surface inclination α is obtained from the latter parametrization. The s coordinate is defined implicitly using the arc length along the surface. Elliptical integrals are involved in its analytical calculation.

The relevant parameters for the two cases are listed in Table 3. The test cases are labelled as "wide" and "tall", referring to the ratio b_{el}/d_{el} of the rail in each case. Both rail cross sections are depicted in Fig. 17. The rail used in test case "wide" is flatter than the circular geometry, such that the surface inclination changes slower across the s direction than for a circular rail. In this case, the rate of change $\partial\alpha/\partial s$ is lowest at the top of the rail and increases towards the sides. Test case "tall", on the other hand, exhibits a faster change of the contact angle than the circular

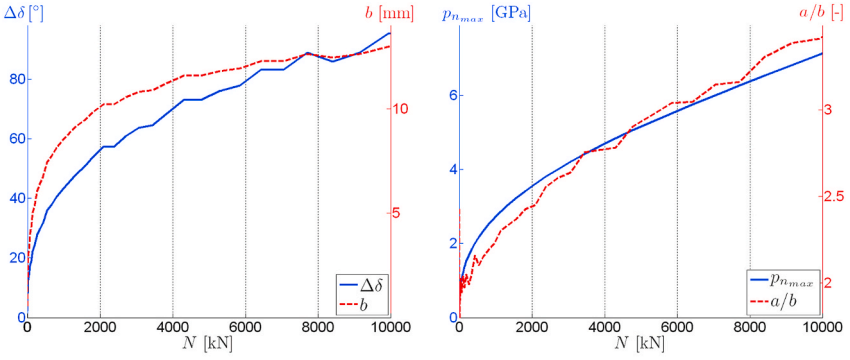

(a) Total contact angle variation $\Delta\delta$ and lateral dimension of contact patch b.

(b) Maximum normal pressure $p_{n_{max}}$ and ratio of longitudinal to lateral dimension of contact patch a/b.

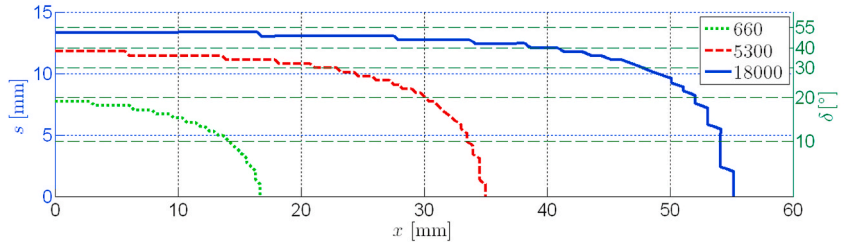

(c) Contact patch contours (symmetric about $x = 0$ and $s = 0$) for $N = 660$, 5 300 and 18 000 kN corresponding to $\Delta\delta \approx 40, 80, 110°$.

Fig. 19. Results of frictionless compression test case "wide" calculated with FEM.

Table 3
Parameters of test cases with different forms of the contact angle variation. The following nomenclature is used: b_{el}/d_{el}: semi-axes of elliptical cross sections in overall lateral/vertical directions; R_{roll}: nominal rolling radius of wheel; E: Young's modulus; ν: coefficient of Poisson; ψ: yaw angle.

	b_{el}/d_{el} [mm]		R_{roll}	Wheel and rail	ψ
	Wheel	Rail	[mm]	material	[mrad]
Case "wide"	13.7/6.49	12.97/6.485	653.7	$E = 210$ GPa;	0
Case "tall"	6.985/14.7	6.485/12.97		$\nu = 0.30$	

geometry at the top of the rail, and a reducing rate of change towards the sides.

The b_{el}/d_{el} ratio of the rail is 2/1 in test case "wide", and 1/2 in test case "tall". The b_{el} and d_{el} dimensions of the wheel have been adjusted in each test case so that the a/b ratios of the longitudinal to lateral dimensions of the resulting contact patches are around the same values in each case. As was shown in Ref. [19], the sensitivity of the contact results to errors in the ICs is higher with higher a/b ratios. Taking this into account, these test cases have been designed with the aim of obtaining contact patches with similar a/b ratios in both of them, to avoid this ratio being an additional factor in the comparisons between both test cases and to allow a more clear interpretation of the new results that are exposed here.

Results computed with FEM. For both test cases, the frictionless contact has been calculated under different loads. The FE contact models have been built with the commercial FE package ABAQUS/Standard [26]. The geometries have been meshed with C3D8 linear hexahedron elements. Fig. 18 shows a detail of the FE mesh for test case "tall". The FE mesh structure for test case "wide" is similar. The surface dimensions of the elements in the most refined zone of each mesh (longitudinal × lateral) are 0.36 × 0.34 mm in test case "wide", and 0.30 × 0.11 mm in test case "tall". Fig. 19 (a), (b) and Fig. 20 (a), (b) show representative results obtained with FEM for the two test cases, such as the contact patch sizes and angle variation, as a function of the compressive normal load N between the contacting bodies. Contact patch shapes are shown in Fig. 19 (c) and Fig. 20 (c) for total angle variations near 40, 80 and 110° in each test case. These are obtained at normal loads $N =$ 660, 5 300 and 18 000 kN for case "wide" and $N = 7.4, 58$ and 310 kN for case "tall". This shows that case "wide", using a flatter rail, requires much bigger loads to produce the same angle variation.

Comparison of FEM with approximate ICs. Fig. 21 concerns the comparison of results computed with FEM and with CECT using the A_{nn}, B_{nn} and $\widehat{B}_{nn}$ ICs for the normal contact problem. The ratios of different results are plotted together for both test cases "wide" and "tall". Using the total contact angle variation $\Delta\delta_{FEM}$ in the abscissa axes, the two cases are compared at equal angle variations rather than at equal normal loads N. For each $\Delta\delta_{FEM}$, the results of different runs for one test case correspond to a same normal load N, different from the load N used in the other test case. The ratio values show the agreement between different runs, with a ratio value of 1 for precise agreement. The FEM results are considered as the reference, although their precision (mostly that of the dimensions of the contact patch) is limited by the mesh resolution for small $\Delta\delta_{FEM}$ values.

The curves $CECT(A)/CECT(\widehat{B})$ of Fig. 21, with the ratios of the results computed with CECT using the A_{nn} and $\widehat{B}_{nn}$ ICs, indicate that the use of the A_{nn} ICs lead to higher errors in case "tall", where the contact angle variation is faster around the central contact point. On the other hand, for $\Delta\delta$ values below 40° the A_{nn} provide good accuracy in the normal contact problem in both cases, with errors limited below 5% in the

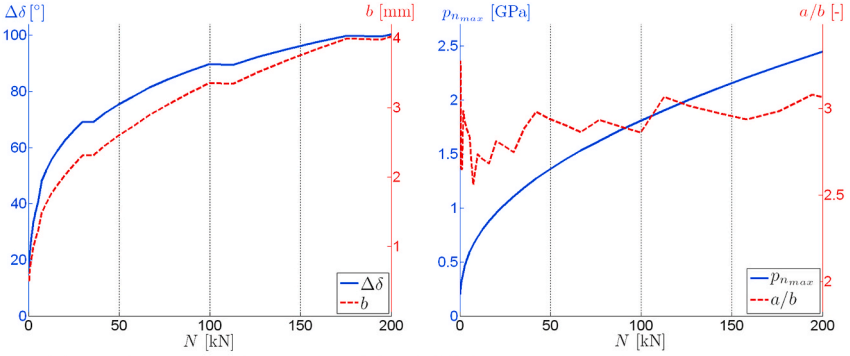

(a) Total contact angle variation $\Delta\delta$ and lateral dimension of contact patch b.

(b) Maximum normal pressure $p_{n_{max}}$ and ratio of longitudinal to lateral dimension of contact patch a/b.

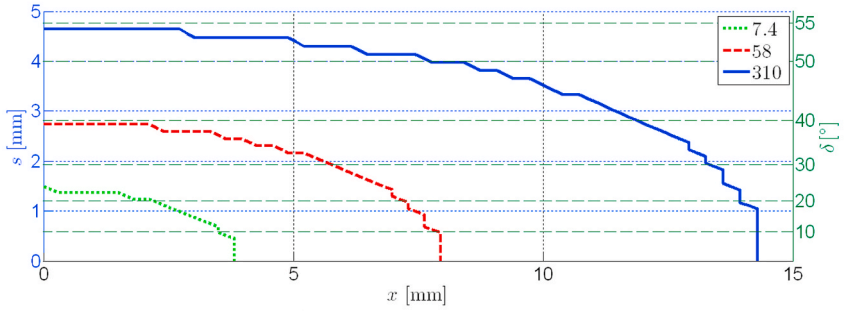

(c) Contact patch contours (symmetric about $x = 0$ and $s = 0$) for $N = 7.4$, 58 and 310 kN corresponding to $\Delta\delta \approx 40, 80, 110°$.

Fig. 20. Results of frictionless compression test case "tall" calculated with FEM.

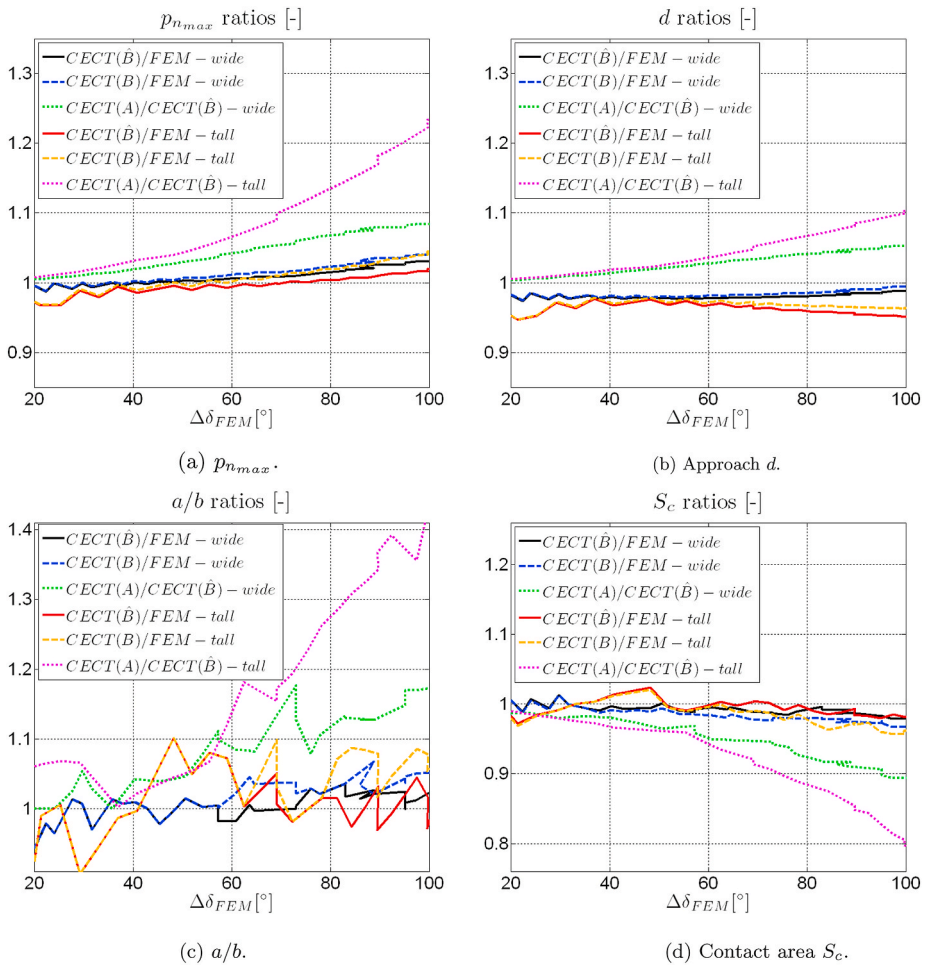

(a) $p_{n_{max}}$. (b) Approach d.

(c) a/b. (d) Contact area S_c.

Fig. 21. Ratios of results of normal contact problem for test cases "wide" and "tall".

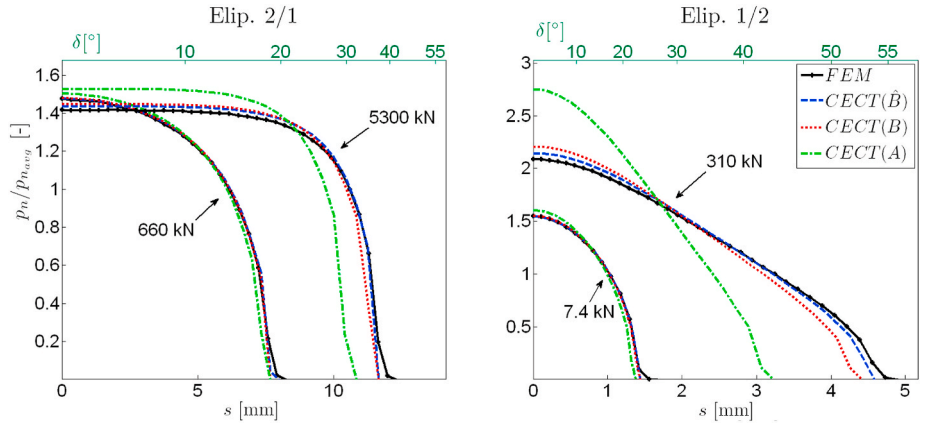

Fig. 22. Non-dimensional normal pressure profiles along s at $x = 0$ for test cases "wide" (left) and "tall" right, for normal loads corresponding to $\Delta\delta \approx 40, 80^\circ$ in test case "wide" and $40, 110^\circ$ in test case "tall". Curves symmetric about $s = 0$.

computed representative quantities. An exception concerns the aspect ratios a/b, where the accuracy of the results is limited more by the mesh resolution.

According to the $CECT(\widehat{B})/FEM$ and $CECT(B)/FEM$ curves in Fig. 21, the B_{nn} and $\widehat{B}_{nn}$ ICs provide good accuracy in both test cases, at least up to $\Delta\delta$ values of 100°. The $\widehat{B}_{nn}$ are more accurate here, except for the approach values computed in case "tall", for which the values obtained with $\widehat{B}_{nn}$ diverge slightly more from those computed with FEM than the values obtained with B_{nn}. It is observed further that the approach values computed with CECT do not converge exactly to the FEM values for low $\Delta\delta$. This is due to the global or "rigid body" displacements contained in the FEM results.

Effects of the pressure distribution. The sensitivity of contact results to errors in the ICs depends, apart from the geometry, also on the stress distributions in the contact patch. The normal pressure profiles at $x = 0$ are plotted in Fig. 22 for the two test cases for two normal loads. The curves are non-dimensionalised with a measure of the average normal

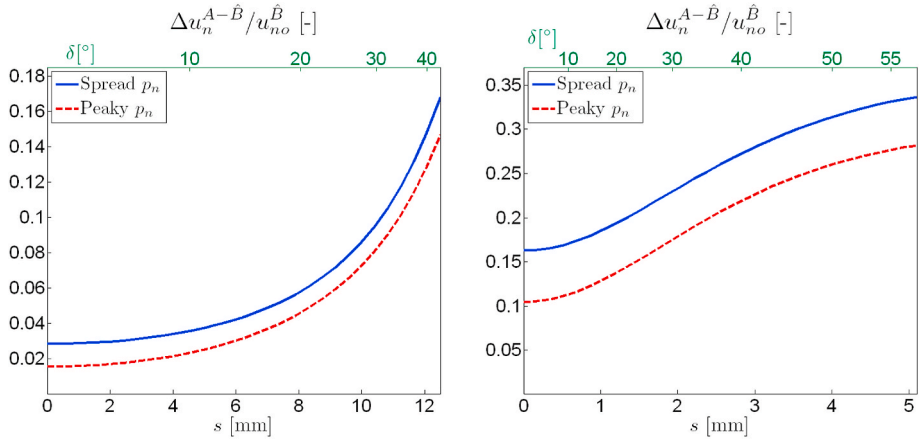

(a) Test case "wide". (b) Test case "tall".

Fig. 23. Non-dimensional differences of normal displacements along s at $x = 0$ computed with A_{nn} and $\widehat{B}_{nn}$ ICs and different normal pressure distributions.

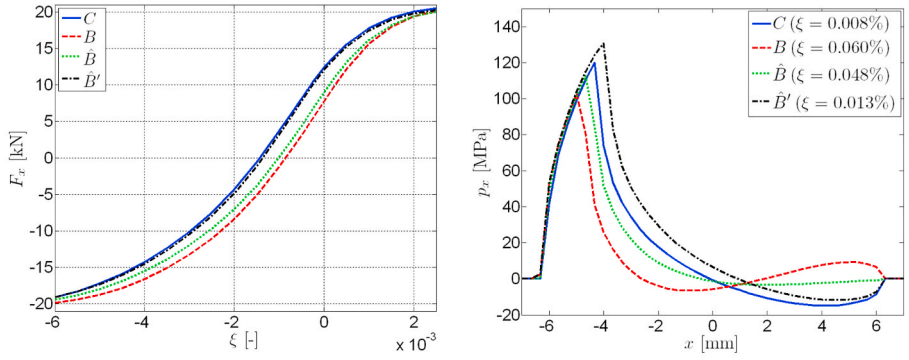

(a) Longitudinal creepage–creep force curve. (b) p_x along x at $s = 0$, for $f_x = 0.65$.

Fig. 24. Performance of approximated ICs in symmetric conformal rolling contact case with $\mu = 0.20$.

pressure for each test case and load, computed as the load N divided by the contact area obtained from the FEM analysis.

Fig. 22 concerns the lateral direction where the pressure profiles deviate from the Hertzian distribution. The distribution evolves into a more uniform distribution for test case "wide", and to a more peaky distribution for test case "tall". This is attributed to the geometries of the two cases, deviating from circular cross-sections. For the wide test-case, the undeformed distance varies less at the centre of the contact and more rapidly towards the sides. The opposite occurs in the tall test-case. A second effect is seen there as well, related to the influence functions, spreading the pressures over a wider region. The pressure profiles maintain shapes close to Hertzian in the longitudinal direction (not shown), in these two test cases with zero yaw angle, becoming just slightly more peaky as the load increases.

The greater spreading of normal pressures in the contact patch in test case "wide" causes an increased sensitivity to errors in the ICs. To show this, the A_{nn} and $\widehat{B}_{nn}$ ICs are used and multiplied with pressure profiles to form normal elastic displacement differences u_n. The two pressure distributions that are considered are those computed with CECT and $\widehat{B}_{nn}$ ICs, corresponding to the highest load levels plotted in Fig. 22 for test case "wide", labelled as "spread p_n", and for test case "tall", labelled as "peaky p_n". The pressure profiles are mapped into the contact patches computed in the same way with CECT and $\widehat{B}_{nn}$ ICs for test case "wide" and $N = 5\,300$ kN ($\Delta\delta \approx 80°$) on the one hand, and for test case "tall" and $N = 310$ kN ($\Delta\delta \approx 110°$) on the other.

Fig. 23 shows a sample of the differences between the u_n's computed with two pressure distributions on the geometry of each test case. These differences between the u_n's are measured in non-dimensionalised form as

$$\Delta u_n^{A-\widehat{B}}(x,s) \overset{def}{=} \left(u_n^A(x,s) - u_n^{\widehat{B}}(x,s)\right) \Big/ \max_{x,s} u_n^{\widehat{B}}(x,s). \tag{18}$$

The superindices in Eq. (18) refer to the I_{nn} with which each u_n are computed.

Comparing the test cases, bigger differences $\Delta u_n^{A-\widehat{B}}$ are observed for case "tall", with a more rapid contact angle variation, than for case "wide". This is in line with the higher errors with the use of the A_{nn} evidenced in Fig. 21 for case "tall". The s-values considered also encompass a bigger $\Delta\delta$ for case "tall" than for case "wide" ($\Delta\delta \approx 110°$ resp. 80°). Further differences are found comparing the pressure distributions in each subfigure. In each geometry, the $\Delta u_n^{A-\widehat{B}}$ are higher with the more spread pressure profile. This proves that for the same errors in the ICs, more spread pressure distributions lead to higher errors in the elastic displacements and hence in the computed contact solution.

As a conclusion, in this section it has been seen how the geometry of the contact surface on the one hand, and the pressure distribution across the contact patch on the other, may affect the precision of the contact results computed with approximate ICs. The errors contained in the A_{nn} and B_{nn} are higher in zones with faster angle variations, and consequently the errors obtained in the solution of the contact problem are higher with geometries in which the contact angle variation is faster

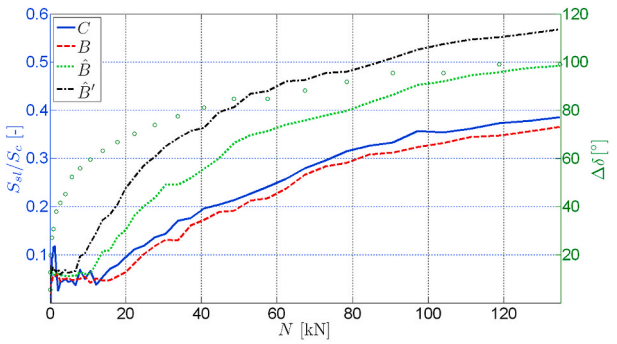

(a) $\mu = 0.40$.

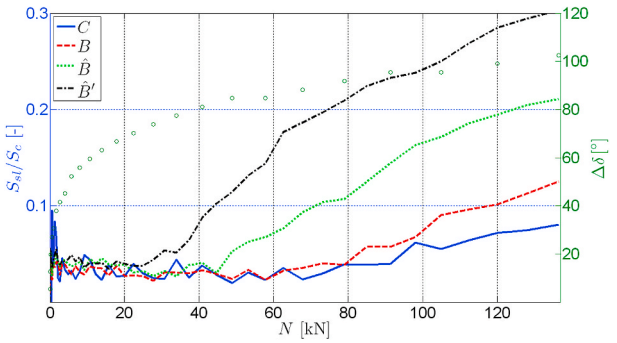

(b) $\mu = 0.60$.

Fig. 25. Comparison of ratios of sliding areas S_{sl} to total contact areas S_c obtained with B and C ICs in a symmetric conformal static compression contact case.

around the central contact point (i.e. the zone in the contact patch with the greatest contributions to the total load). It has been seen as well that a more uniform pressure distribution across the contact patch increases the sensitivity to errors in the ICs.

6.2. Tangential contact

To assess the precision of different variants of approximated ICs in the tangential part of the contact problem, the frictional contact of a concave wheel on a convex rail is considered here. Three different values of constant coefficients of friction are used, namely $\mu = 0.20$, 0.40 and 0.60. Geometry 2 of Table 1 is considered, except that the circular cross sectional profile of the wheel is replaced with an elliptical one with semi-axes b_{el} and d_{el} of 10.15 and 10.25 mm respectively, close to the original. This modifies the shape of the wheel surface only very slightly, such that the C_{ij} presented in Section 5 continue to be valid. The change does however significantly alter the normal undeformed distance to the rail, making the normal pressure distribution more evenly distributed in the lateral direction.

Fig. 24 summarizes results obtained with $\mu = 0.20$ for the laterally symmetric rolling contact with a total normal load N of 100 kN, zero yaw angle and zero lateral rigid slip at the central contact point. Results are shown for B, $\widehat{B}$ and $\widehat{B}'$ approximated ICs, along with those obtained with the C ICs that are considered the reference solution. These results may be compared with the ones shown in [19, Fig. 14], for a similar geometry and different N and μ.

Fig. 24a shows the longitudinal creep force curves obtained with the different sets of ICs. Significant offsets are shown for the B and $\widehat{B}$ ICs that are attributed to the differential stiffness effect between the convex and concave bodies. This offset is well compensated by the adjustment between the $\widehat{B}'_{xn}$ and the C_{xn}, cf. Fig. 12. The adjustment parameters for the $\widehat{B}'$ ICs used here are those listed in Table 2 for geometry 2. These yield a creep force curve that is in close correspondence to the reference obtained with the C ICs.

The patterns of longitudinal tangential stress p_x computed with the $\widehat{B}'$ ICs are also improved, as illustrated in Fig. 24b. This figure shows the p_x profiles along the centreline of the contact patch obtained with different sets of ICs, for the same value of longitudinal traction ratio $f_x = F_x/\mu F_n$. The longitudinal creepage values ξ at which this f_x is obtained are indicated in the legend of the graph for each set of ICs.

For higher values of μ, the differences between the results obtained in the tangential part of the contact problem for this rolling contact case with the different sets of ICs diminish. This happens because the influence of the normal pressures on the tangential contact problem is proportionally lower with higher μ and tangential stresses, and hence the role of the I_{xn} gets less important.

Previously, Fig. 15 showed that the $\widehat{B}$ and $\widehat{B}'$ ICs provide a worse approximation of the C_{sn} than the B ICs. As the C_{sn} are greater in magnitude than the C_{xn}, this may affect the tangential part of the contact problem significantly, especially in problems in which larger rigid slips in s direction occur. A problem where this happens is the static normal compression between a convex and a concave body with zero shift in longitudinal direction. This is computed for the same geometry and coefficients of friction as in the previous rolling contact case.

The result that is shown in Fig. 25 is the ratio of area in sliding S_{sl} to total contact area S_c, as a function of the total compressive load N (sum of the resultants of the normal and tangential stresses in the contact patch), monotonically increasing, for $\mu = 0.40$ and $\mu = 0.60$. With $\mu = 0.20$ the differences between the sliding areas obtained with the different sets of ICs are attenuated in this case due to the higher saturation level.

The $\Delta\delta$ spanned by the contact patch as a function of the load (as computed with the C ICs) is shown in each subfigure with circle markers. Clearly, the B ICs provide the results closest to the C ICs, while the adjusted $\widehat{B}'$ ICs provide the worst results. This suggests that the adjustment for the differential stiffness effect, intended for the improvement of the B_{xn}, should not be applied in the B_{sn}. Furthermore, the B_{sn} provide a better approximation of the C_{sn} than the $\widehat{B}_{sn}$, and consequently more precise results are obtained in the tangential part of the contact problem with the B_{sn} than with the $\widehat{B}_{sn}$.

7. Conclusions

Precise ICs are not readily available for general non-planar solids, and they must be generally obtained through numerical calculation. This involves a notable difficulty for the application of the exact contact theory in conformal contact problems, especially when precise results are sought with moderate or high conformity levels considering the tangential part of the contact problem. Different possibilities are explored for approximate analytical computation, by which this difficulty may be alleviated, and numerical calculation of ICs can be avoided as much as possible.

This work presented new variants for the approximation of ICs of non-planar solids based on surface orientations, and an extension to incorporate the effect of the geometric differential stiffness between convex and concave conforming solids, based on the definition of spatially variable modified elastic properties of the solids. A fundamental assumption of the studied approximations is that the contacting solids may be considered approximately prismatic around the contact, as it happens in relevant rolling contact applications like the wheel–rail case or in rolling bearings. The different approximated ICs have been compared with two sets of numerically calculated ICs, and their performance has been assessed in the normal and tangential parts of the contact problem.

The new $\widehat{B}$ variant of approximated ICs appears to slightly improve the approximation of the C_{nn} ICs with respect to the original B ICs, and

provides better results in the normal part of the contact problem. On the other hand, the B_{sn} approximate the C_{sn} better than the $\widehat{B}_{sn}$. The extension for the geometric differential stiffness effect gives a considerable improvement in the approximation of the C_{xn}. However, the associated parameter adjustment is empirical, and necessitates some numerically calculated C_{xn} as reference. Additionally, this extension has currently been verified to work well only with the $\widehat{B}_{xn}$.

Accounting for these results, the best choice of approximated ICs could be to use the $\widehat{B}$ ICs, except for the I_{sn}, where the B ICs seem to perform better. The $\widehat{B}_{xn}$ should be adjusted for the differential stiffness effect whenever possible; failing this, the direct use of the half-space A_{xn} is preferred over the different variants of B_{xn}. Despite their low magnitude, they have a considerable influence on the longitudinal tangential stresses, and use of inaccurate I_{xn} may lead to a significant offset in the longitudinal creep force curve. The I_{ns} and I_{nx} ICs can be defined according to the selected I_{sn} and I_{xn} ICs to fulfill reciprocity exactly. These ICs are of less importance because the normal displacements are generally dominated by the normal pressures.

For the propagation of errors in the solution of contact problems, it is shown that geometries with faster contact angle variations are more prone to errors in the normal contact solution due to the higher errors contained in the approximated ICs, and that the sensitivity to errors in the ICs increases when the contact pressures are more spread out in the lateral direction of the contact patch. For the tangential part of the contact problem, it is shown once more that relatively small errors in the I_{sn} and I_{xn} ICs may lead to appreciable differences in the results.

The current study has focused on contact between bodies with elastically similar materials. Significant differences are noted between the individual ICs of separate non-planar solids, I^i_{xx} and especially I^i_{ss}, that are of primary importance in the tangential contact problem. The errors in these individual ICs are of opposite signs in the convex and concave bodies and tend to be cancelled out in the combined ICs. The extent of this compensation depends on the relative stiffness of both bodies, and may not be sufficiently favourable especially when the convex body is the one with the more flexible material. In that case, the approximation of these ICs should be improved further.

CRediT authorship contribution statement

Julio Blanco-Lorenzo: Conceptualization, Methodology, Software, Investigation, Writing - original draft. **Edwin A.H. Vollebregt:** Conceptualization, Validation, Formal analysis, Writing - review & editing. **Javier Santamaria:** Conceptualization, Resources, Supervision, Project administration, Funding acquisition. **Ernesto G. Vadillo:** Conceptualization, Resources, Supervision, Project administration, Funding acquisition.

Declaration of competing interest

The authors declare that they have no known competing financial interests or personal relationships that could have appeared to influence the work reported in this paper.

Acknowledgements

This work has been partly financed within the European Horizon 2020 Joint Technology Initiative Shift2Rail, through contract no. 826255 (IN2TRACK2). The authors wish to thank as well the Spanish Research Ministry MICINN/Economy and Competitiveness Ministry MINECO and MCI/AEI for their funding through contracts TRA2014-59599-R and PID2019-109483RB-I00, including funding by the FEDER-ERDF European Regional Development Fund, and also the Basque Government for financial assistance through IT919-16.

References

[1] Liu Y, Liu L, Mahadevan S. Analysis of subsurface crack propagation under rolling contact loading in railroad wheels using FEM. Eng Fract Mech 2007;74:2659–74.
[2] Pletz M, Daves W, Yao W, Ossberger H. Rolling contact fatigue of three crossing nose materials – multiscale FE approach. Wear 2014;314(1–2):69–77.
[3] Vo KD, Tieu AK, Zhu HT, Kosasih PB. A 3D dynamic model to investigate wheel-rail contact under high and low adhesion. Int J Mech Sci 2014;85:63–75.
[4] Zhao X, Zhang P, Wen Z. On the coupling of the vertical, lateral and longitudinal wheel–rail interactions at high frequencies and the resulting irregular wear. In: Li Z, Núñez A, editors. Proceedings of the 11th international conference on contact mechanics and wear of rail/wheel systems. The Netherlands: Delft University of Technology; 2018.
[5] Lian Q, Deng G, Tieu AK, Li H, Liu Z, Wang X, Zhu H. Thermo-mechanical coupled finite element analysis of rolling contact fatigue and wear properties of a rail steel under different slip ratios. Tribol Int 2020;141.
[6] ANSYS. Contact technology guide. release 12.1. ANSYS, Inc.; 2009.
[7] Kalker JJ. Survey of wheel-rail rolling contact theory. Veh Syst Dyn 1979;8(4):317–58.
[8] Kalker JJ. Three-dimensional elastic bodies in rolling contact, volume 2 of Solid Mechanics and its Applications. Dordrecht, Netherlands: Kluwer Academic Publishers; 1990.
[9] Vollebregt EAH. User guide for CONTACT, Rolling and sliding contact with friction. 2020. Technical Report 20-01, version 20.2, Vtech CMCC, www.kalkersoftware.org.
[10] Vollebregt EAH. Detailed wheel/rail geometry processing using the planar contact approach. Vtech CMCC; 2020.
[11] Jin X, Wen Z, Zhang W, Shen Z. Numerical simulation of rail corrugation on a curved track. Comput Struct 2005;83:2052–65.
[12] Baeza L, Fuenmayor FJ, Carballeira J, Roda A. Influence of the wheel-rail contact instationary process on contact parameters. J Strain Anal 2007;42:377–87.
[13] Kaiser I. Refining the modelling of vehicle-track interaction. Veh Syst Dyn 2012;50(Suppl):229–43.
[14] Li Zili. Wheel-rail rolling contact and its application to wear simulation. PhD thesis. Delft University of Technology; 2002.
[15] Vollebregt EAH, Segal A. Solving conformal wheel-rail rolling contact problems. Veh Syst Dyn 2014;52(suppl. 1):455–68.
[16] Vollebregt EAH. Conformal contact: corrections and new results. Veh Syst Dyn 2018;56(10):1622–32. https://doi.org/10.1080/00423114.2018.1424917.
[17] Vollebregt EAH. Detailed wheel/rail geometry processing using the conformal contact approach. Multibody Syst Dyn 2020. Accepted for publication.
[18] Blanco-Lorenzo J, Santamaria J, Vadillo EG, Correa N. On the influence of conformity on wheel-rail rolling contact mechanics. Tribol Int 2016;103:647–67.
[19] Blanco-Lorenzo J, Santamaria J, Vadillo EG, Correa N. A contact mechanics study of 3D frictional conformal contact. Tribol Int 2018;119:143–56.
[20] Zhao J, Vollebregt EAH, Oosterlee CW. Extending the BEM for elastic contact problems beyond the half-space approach. Math Model Anal 2016;21(1):119–41.
[21] Sundaram N, Farris TN. Mechanics of advancing pin-loaded contacts with friction. J Mech Phys Solid 2010;58:1819–33.
[22] van der Wekken CD, Vollebregt EAH. Numerical calculation of the elastic field in a half-space using bilinear elements. Math Mech Solid 2019;24:3537–53.
[23] Flamant A. Sur la répartition des pressions dans un solide rectangulaire chargé transversalement. Compte. Rendu. Acad. Sci. 1892;114:1465 [Paris].
[24] Woodward W, Paul B. Contact stresses for closely conforming bodies – application to cylinders and spheres. University of Pennsylvania; 1976. Technical Report DOT-TST-77-48.
[25] Titovich AS, Norris AN. Green's function for symmetric loading of an elastic sphere with application to contact problems. J Mech Mater Struct 2012;7(7):701–19.
[26] Abaqus analysis user's manual. Version 6.12. Dassault Systèmes Simulia Corp.; 2012.